Bulletin of the New Zealand Society for Earthquake Engineering, Vol. 59, No. 1, March 2026

SEISMIC ENHANCEMENT OF COMMUNITY HOUSINGS IN NEPAL'S MID-HIMALAYAS: RETROFITTING AND RECONSTRUCTION SCENARIOS

Magnus Upadhyay[1], Pradeep Kafle[1], Sabin Ban[2] and Shreedhar Khakurel[3*]

(Submitted *February 2025*; Reviewed *April 2025*; Accepted *August 2025*)

ABSTRACT

Nepal lies within the Himalayan seismic belt, making it one of the most earthquake-prone regions globally. Non-engineered masonry structures, though widely used, are highly vulnerable to seismic disasters. Replacing these structures is impractical and culturally insensitive due to their deep traditional and cultural significance. Retrofitting is a practical and culturally appropriate approach to enhance a building's strength and safety against earthquakes. This study evaluates retrofitting and reinforcement techniques for unreinforced masonry (URM) structures in Nepal's mid-Himalayan region through numerical modelling, non-linear static analysis, and fragility assessment. Pushover analysis revealed that reconstruction models significantly improve base shear capacity compared to the URM model. Although gabion wire retrofitting has a limited effect at the initial stage, it significantly improves strength at larger displacements. Vertical reinforcements and horizontal bands in the reconstruction model consistently enhance performance. The URM model exhibits concentrated cracking near openings and corners, while the retrofitted model improves stress distribution and reduces crack widths. Additionally, the reconstruction model confines cracks within bands, preventing vertical propagation and ensuring superior structural integrity. Fragility curves reveal that reinforcement significantly enhances seismic performance, as the retrofitted model improves resistance across damage states, with exceptional collapse resistance due to its ductility, allowing energy absorption and delayed failure. The reconstruction model offers consistent protection with lower probabilities of damage across all states, underscoring its reliability during seismic events. Although the reconstruction model incurs higher costs than the retrofitted model due to its extensive reinforcement features, both models provide substantial seismic benefits compared to the base URM model.

https://doi.org/10.5459/bnzsee.1733

INTRODUCTION

Nepal, situated in the central 800 km stretch of the Himalayan seismic belt, is one of the most earthquake-prone regions in the world [1]. Between 1255 AD and the present, five major earthquakes have been documented in this region: the Mw 7.7 Kathmandu earthquake in 1255, the Mw 8.2 Mustang earthquake in 1505, the Mw 7.6 Nepal earthquake in 1833, the Mw 8.1 Bihar-Nepal earthquake in 1934, and the Mw 7.8 Gorkha earthquake in 2015 [2]. The 2015 earthquake destroyed more than 600,000 buildings, and about 95% of the completely collapsed structures were low-strength masonry buildings, as shown in Table 1 [3]. These statistics highlight the extreme vulnerability of Nepal's traditional masonry structures, particularly in its mid-Himalayan settlements, where non-engineered construction remains prevalent [4].

Table 1: Damage due to the 2015 Gorkha earthquake based on building typology [3].

SN	Building Typology	Fully Damaged	Partially Damaged
1	Low-Strength Masonry	474,025 (95%)	173,867 (67.7%)
2	Cement-Based Masonry	18,214 (3.7%)	65,859 (25.7%)
3	Reinforced Concrete Frame	6,613 (1.3%)	16,971 (6.6%)
	Total	498,852	256,697

A similar pattern of seismic vulnerability has been observed in various regions with large stocks of unreinforced masonry (URM) buildings [5-7]. A study by Ismail et. al. [5] found that 680 out of 750 existing unreinforced masonry (URM) buildings in Dunedin, New Zealand, were expected to have their seismic capacity exceeded even under moderate earthquake shaking, primarily due to their construction before the implementation of modern seismic codes. In Nepal's mid-Himalayan region, a large number of rural buildings were similarly built without adherence to seismic design standards, reflecting comparable construction practices that give rise to similar vulnerabilities despite differing seismic demands. However, unlike New

[1] *Pashchimanchal Campus, Institute of Engineering, Tribhuvan University, Nepal.*
[2] *National College of Engineering, Institute of Engineering, Tribhuvan University, Nepal.*
[3] *Corresponding Author, Assistant Professor, Pashchimanchal Campus, Tribhuvan University, Nepal. shreedhar.khakurel@ioepas.edu.np*

Zealand, where detailed assessments and mitigation strategies are actively pursued, Nepal faces additional challenges due to financial constraints, lack of awareness, and a cultural preference for traditional construction methods. Nevertheless, earthquake-resilient buildings are achievable using locally available materials such as stone, mud, and timber, especially when traditional construction techniques are employed in conjunction with scientifically validated seismic-resilient features [8].

In many developing countries, including Nepal, non-engineered masonry construction is widespread due to its low cost, availability of materials, and traditional building practices [9]. However, the vulnerability of such structures poses significant risks during seismic events. Replacing these buildings with modern earthquake-resistant alternatives is not always feasible due to economic limitations and the deep cultural and historical value these structures hold [10]. As a result, retrofitting has emerged as a practical alternative that strengthens existing buildings while preserving their architectural and functional integrity. Despite this, many homeowners opt for demolition and reconstruction rather than retrofitting due to misconceptions about its complexity, cost, and effectiveness [11].

A clear distinction must be made between repair, restoration, and retrofitting. Repair primarily focuses on superficial fixes to restore a building's appearance and usability without addressing structural weaknesses [12]. Restoration, while aiming to return a structure to its pre-damage condition, often does not enhance seismic performance. In contrast, retrofitting reinforces a building's structure, fixes its weaknesses, and makes it better able to resist future earthquakes [12]. Retrofitting not only enhances the seismic resilience of masonry buildings but also extends their service life, ensuring safety and durability.

Among various retrofitting techniques, reinforced concrete/ ferrocement wall jacketing and splint-and-bandage methods using steel bars or wire (GI) mesh, and GI wire mesh jacketing have proven to be among the most effective and economically viable solutions [13-15]. The GI wire mesh jacketing technique creates a continuous reinforcement cage around masonry walls, significantly improving their ductility and resistance to lateral forces. This method is lightweight, cost-effective, and adaptable to various building geometries, making it highly suitable for Nepal's rural settlements. Additionally, studies indicate that retrofitting has approximately 60% lower environmental impact compared to constructing new stone masonry structures, making it a more sustainable approach [16].

Despite its advantages, retrofitting remains underutilised in Nepal's mid-Himalayan region due to challenges such as limited experience and research on strengthening low-strength masonry buildings, which are prevalent in rural areas. This has led to a lack of confidence among stakeholders, often resulting in the demolition of partially damaged structures in favour of full reconstruction [17]. The cost of retrofitting using GI welded wire mesh is approximately $5–7 per square foot, while new construction costs around $20 per square foot [13], though these figures are based on older data and may not reflect current prices. This significant cost difference makes retrofitting a more economical option, yet misconceptions about effectiveness persist mostly due to a lack of experience and research [17]. Additionally, a lack of technical knowledge and community-level implementation examples has hindered its widespread adoption. However, cost-benefit analyses have demonstrated that the reduction in future earthquake-induced losses far outweighs the initial investment, making retrofitting a financially sound decision [18]. Moreover, recent advancements in low-damage technologies focus on repairable structural systems that minimize post-earthquake downtime and economic loss [19].

This study aims to compare a macro-model of an existing unreinforced stone masonry (URM) building structure with its retrofitted counterpart and a reinforced model representing new construction that incorporates modern seismic elements as presented in NBC 202: 2015 [20].

METHODOLOGY

Building Description

The building is situated in Lwang Village, Kaski District, Nepal, which lies in the mid-Himalayan region. The village is home to numerous community housing structures that not only serve as residences but also support local economies through homestay tourism, which allows tourists to experience the traditional lifestyle of the community. Past studies have shown that the structures in the region are vulnerable to earthquakes [7,21]. Further, it is a typical two-storey high stone-mud masonry structure with a plan dimension of 10.9 metres by 6.12 metres and a height of 5.3 metres. The building was constructed using traditional materials and techniques commonly used in the region. The walls are constructed from semi-dressed stone as masonry units and mud mortar, the flooring is made of *Chilaune* wood (Schima wallichii) and mud, and the roofing consists of stone and metal sheets. Notably, the structure lacks essential seismic features such as horizontal bands, corner reinforcements, and vertical stitches, which are critical for enhancing seismic resilience. The use of local materials, traditional building architecture, absence of seismic features, and vulnerability to seismic events make the building an ideal candidate for evaluating potential retrofitting measures to improve its earthquake resistance. Figure 1 shows the photograph, elevation, and plan of the representative building (all dimensions are in metres).

Numerical Modelling

To evaluate the seismic performance of traditional stone masonry buildings and assess the effectiveness of proposed interventions, three-dimensional finite element-based numerical models (macro-models) were developed using the displacement analyser finite element analysis (DIANA FEA10.5) software [22]. Three models were analysed: (i) the unreinforced stone masonry building (URM) as a baseline (Figure 2a), (ii) a stone masonry building retrofitted with gabion wire jacketing (JM), designed to evaluate performance improvements for existing structures (Figure 3a), and (iii) a stone masonry building with vertical reinforcements for junction and corner strengthening, and seismic bands at sill, lintel, and roof levels (RM) (Figure 4a) to assess the performance of new masonry houses constructed according to NBC 202: 2015 [20] provisions. These models provided a comparative framework to examine unreinforced, retrofitted, and new construction scenarios under seismic conditions.

The base model (URM) consists of stone units and mud mortar, forming a stone-mud masonry structure. It also includes a timber beam and timber floor with loose connections, which act as a flexible diaphragm. This model has no specific seismic resisting elements. The second model (JM) introduces a retrofitting technique utilising gabion wire mesh to enhance the seismic resilience of the structure. The mesh, with a diameter of 2 mm, is arranged in a grid pattern with a centre-to-centre spacing of 150 mm, both horizontally and vertically, as shown in Figure 5 (a), ensuring uniform reinforcement across the masonry walls. This retrofitting method is designed to provide additional confinement to the masonry, thereby improving its ductility and mitigating seismic vulnerabilities. This retrofitting approach is inspired by the example provided in the seismic retrofitting guidelines of masonry buildings in Nepal [12]. For determining the spacing of the gabion wire, it is assumed that the lateral load is resisted solely by the gabion wire mesh;

however, the numerical model considers the combined contribution of both the masonry and the gabion wire in resisting the load. Additionally, a 25% reduction in the strength of the gabion wire mesh was considered to account for potential degradation or weaknesses due to knotting of the GI wire, as specified in the guidelines for masonry structures [12].

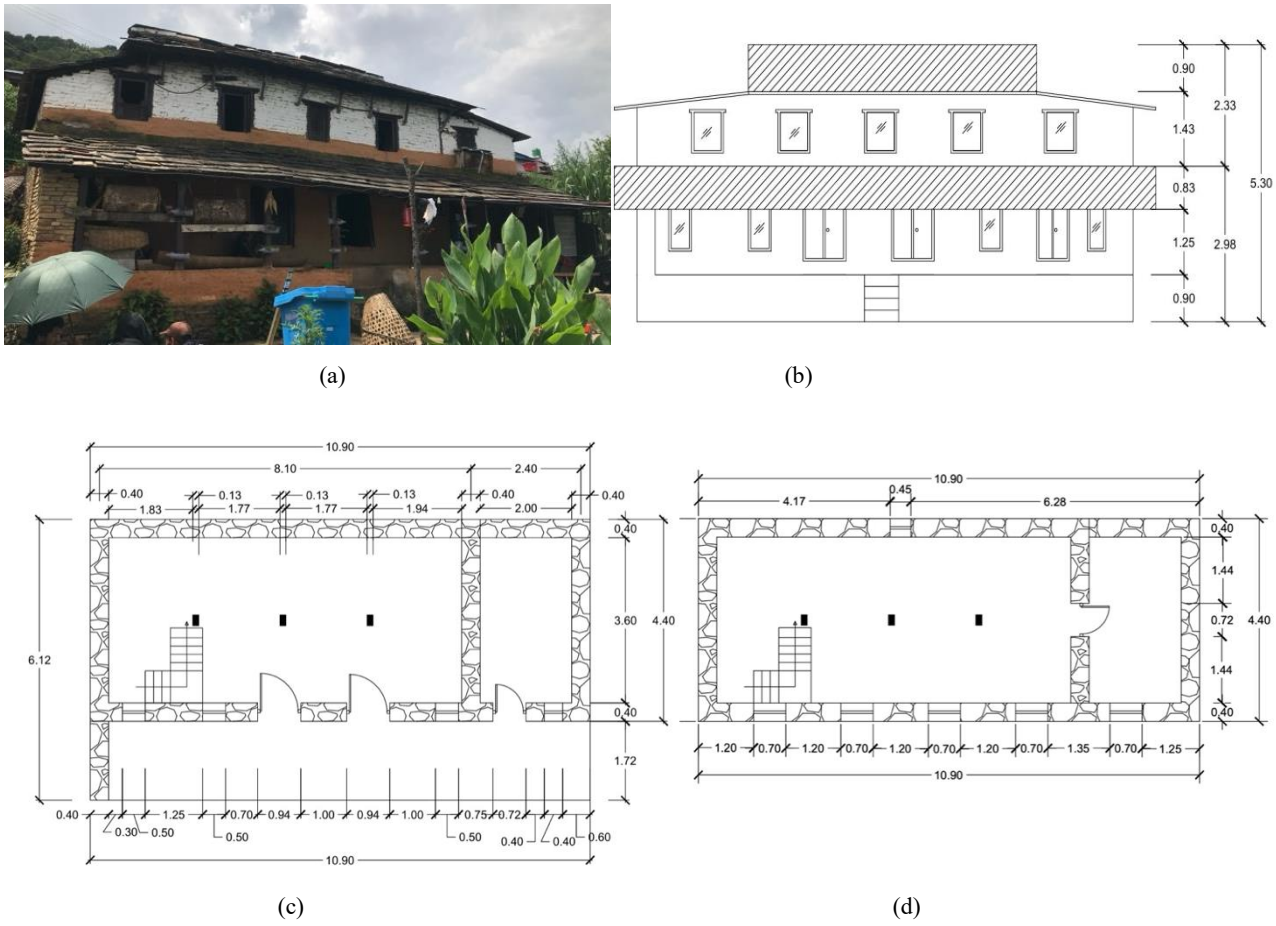

(a) (b)

(c) (d)

Figure 1: (a) Representative Building, (b) Elevation, (c) Ground floor plan, and (d) First floor plan of the representative building.

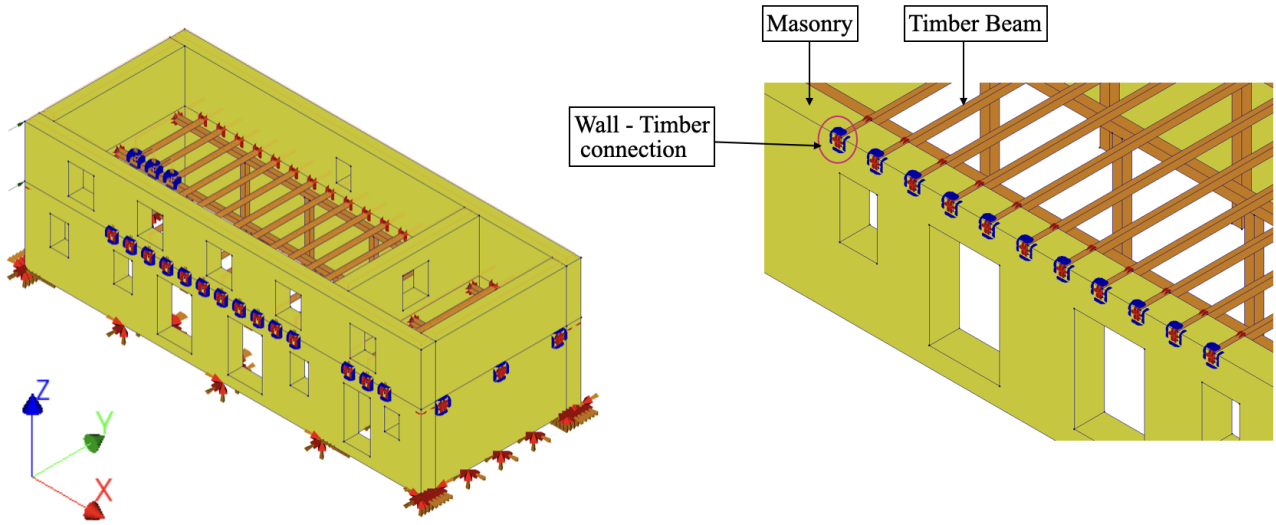

(a) (b)

Figure 2: a) URM model, and b) Wall-Timber Interface.

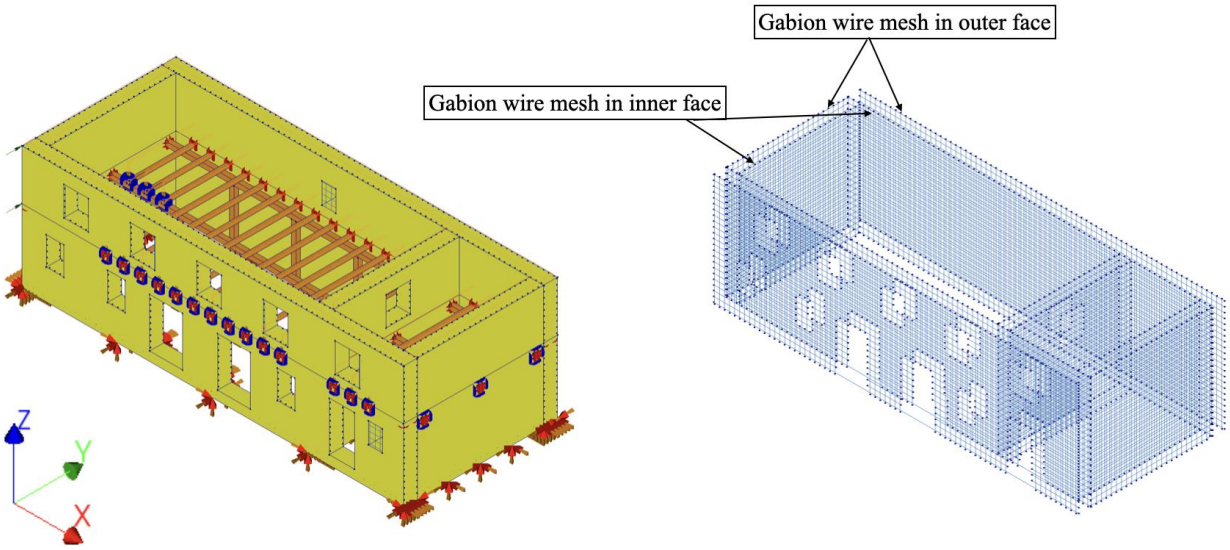

(a) (b)

Figure 3: a) JM model, and b) Gabion wire mesh adopted in JM model.

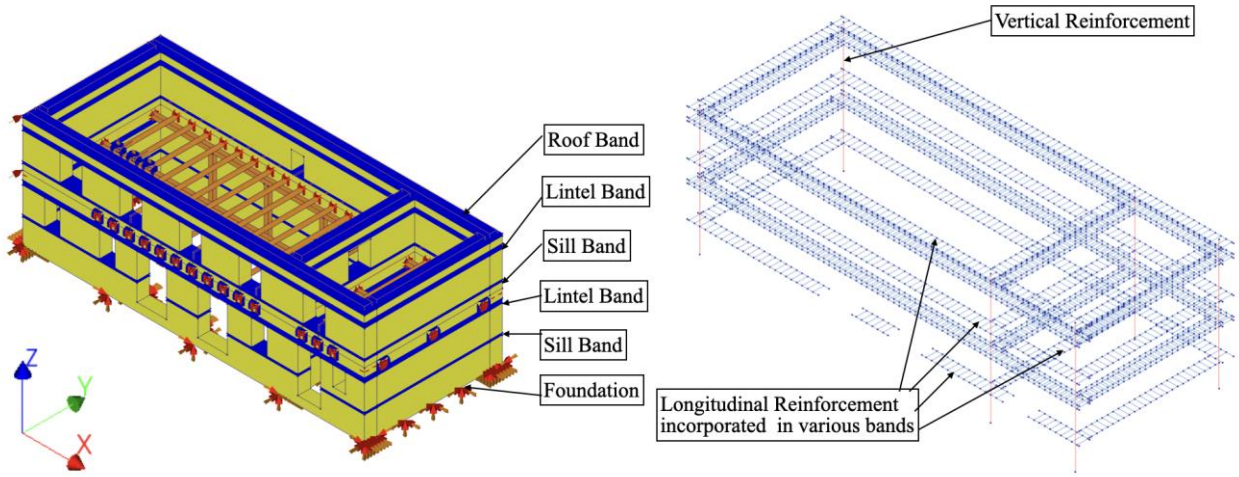

(a) (b)

Figure 4: a) RM model, b) Reinforcement in sill band, lintel band, and roof band adopted in RM model.

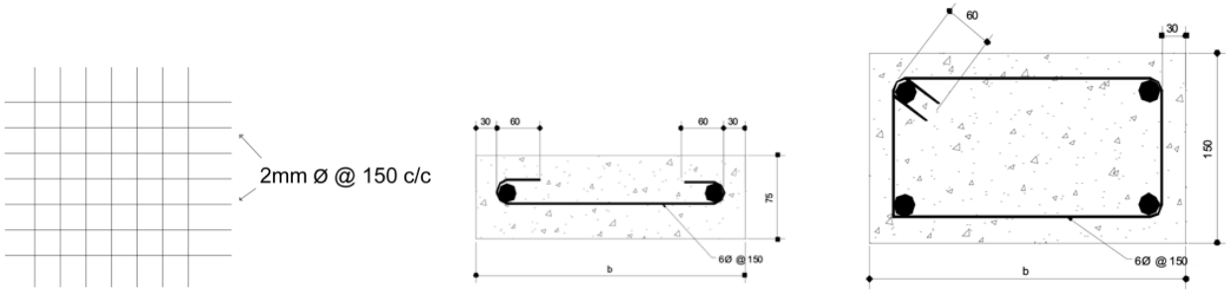

(a) (b) (c)

Figure 5: a) Gabion wire reinforcement detail, b) Sill and Roof bands detailing [20], c) Lintel band [20].

The third model (RM) represents a reinforced scenario designed to enhance the seismic performance of traditional stone masonry structures through the incorporation of modern reinforcement techniques. Sill, lintel, and roof bands were constructed using M20 grade concrete (28th day characteristic compressive strength of standard cube is 20 MPa), reinforced with Fe415 steel (yield strength = 415 MPa), and included 6 mm diameter links placed at 150 mm centre-to-centre spacing. In addition to these elements, one vertical reinforcement bars of 16 mm diameter were placed at each wall junctions. However, it is important to note that the effectiveness of these vertical rebars depends significantly on proper bonding at wall junctions, which, if inadequate, can compromise their performance [23]. This model was specifically studied to understand the role and effectiveness of seismic elements in newer constructions and to enable a direct comparison with both the retrofitted model (representing existing structures) and the existing unreinforced structure. The reinforcement details

and configurations are summarised in Table 2, while the accompanying Figures 5 (b) and (c) illustrate the cross-sectional arrangement of the sill, roof, and lintel bands (all dimensions are in mm). This analysis provides valuable insights into the benefits of incorporating modern seismic provisions in masonry buildings. As the focus of this study is on the in-plane behaviour of masonry walls and the effectiveness of gabions wire mesh jacketing and seismic elements in newer constructions, the roof structure is not explicitly modelled. However, its weight is calculated and applied as a uniformly distributed load along the top of the walls. This modelling approach assumes that out-of-plane wall behaviour and local failure mechanisms are restrained, which is a limitation of the current study.

Table 2: Band Detailing [20].

Bands	Thickness	Number of Reinforcing bars	Diameter
Sill	75 mm	2	12 mm
Lintel	150 mm	4	12 mm
Roof	75 mm	2	12 mm

The numerical models consist of material and element definitions to accurately simulate the structural behaviour. Walls were modelled using solid elements classified as structural solids, with the Total Strain-Based Crack Model for material behaviour, employing a rotating crack orientation. Tensile behaviour followed an exponential curve with crack bandwidth specified as Rots, while compressive behaviour was represented by a parabolic curve. Timber components were also modelled as solid elements with linear elastic properties. Gabion wire mesh and reinforcement bars for seismic bands were represented using line elements with a Von Mises plasticity material model, incorporating isotropic hardening defined by plastic strain-yield stress relations as shown in Figure 6.

Concrete bands were modelled as solid elements with the Total Strain-Based Crack Model, using similar tensile and compressive behaviour definitions as the walls. To capture the interaction between masonry walls and timber beams, as shown in Figure 2b, a structural plane interface element was used, with behaviour modelled using Coulomb-friction parameters to address the connection. Material properties adopted in the modelling are presented in Table 3.

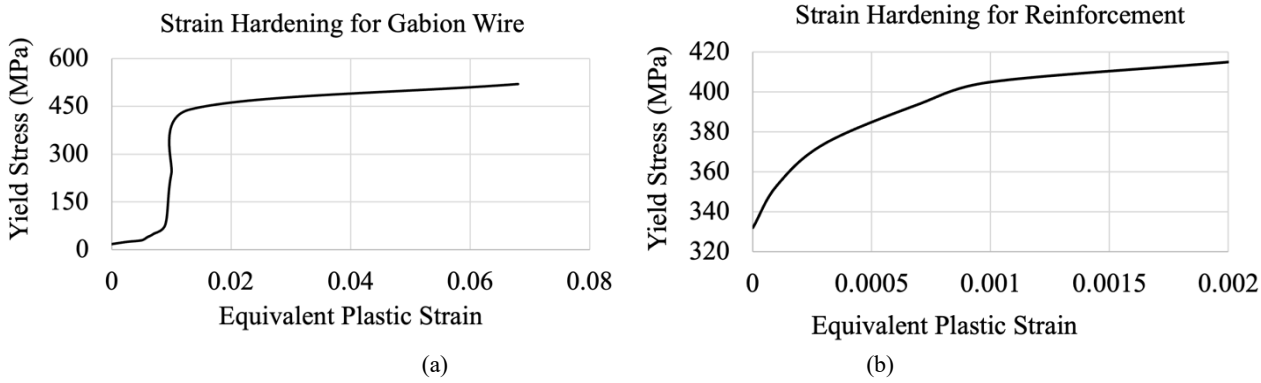

Figure 6: Strain Hardening plot for a) Gabion wire [24] and b) Fe415 rebar adopted in the finite element model [22].

Table 3: Material properties adopted in the finite element model.

Parameters	Stone Mud Masonry	Concrete	Timber	Steel	Gabion Wire	Wall-Timber Interface
References	[25]	[26]	[27]	[26]	[24]	[28]
Young's Modulus of Elasticity (E): MPa	65.1	22360.7	9,570	2,00,000	1,30,000	-
Poisson's Ratio	0.25	0.2	0.3	-	-	-
Mass Density: Kg/m^3	2200	2500	693	-	-	-
Tensile Strength: MPa	0.02	2.2	-	-	-	-
Tensile Fracture Energy: N/m	2	220	-	-	-	-
Compressive Strength: MPa	2.4	20	-	-	-	-
Compressive Fracture Energy: N/m	240	2000	-	-	-	-
Normal Stiffness Modulus: N/mm^3	-	-	-	-	-	100
Shear Stiffness Modulus: N/mm^3	-	-	-	-	-	50
Cohesion: N/mm^3	-	-	-	-	-	0.55
Frictional angle: Radian	-	-	-	-	-	0.51

Analysis

The analysis was conducted using the finite element software DIANA FEA 10.5 to evaluate the seismic performance of the structure. Initially, an eigenvalue analysis was performed to determine the fundamental vibration modes and natural frequencies, providing essential insights into the structure's dynamic characteristics. Following this, a nonlinear static (pushover) analysis was carried out to assess the structural capacity under incremental lateral loads. The analysis was carried out in both X-direction (along the longer length) and Y-direction (along the shorter length) as suggested by Ban et. al. [29]. The analysis accounted for both physical (material) and geometric nonlinearities, with initial conditions continuing from a gravity load case. A displacement-controlled load was applied at the storey level in proportion to the storey height, with a target displacement of 80 mm. The iterative solution process utilised the Secant (Quasi-Newton) method with a maximum of 50 iterations and a convergence tolerance of 0.5, employing the Parallel Direct Sparse solver. This analysis produced a capacity curve, depicting the relationship between base shear and roof displacement and reflecting the overall structural performance under lateral loads.

To evaluate seismic demand and performance, the equations as outlined in ATC 40 [30] guidelines and procedures as outlined in Otani et.al. [31] were applied. The capacity curve from the pushover analysis was transformed into a capacity spectrum in the spectral acceleration-spectral displacement domain as shown in Figure 7. Simultaneously, the response spectrum for Soil Type A, defined in NBC 105 2020 [32], was converted into a demand spectrum using Equations 1, 2 and 3 [30] as shown in Figure 8.

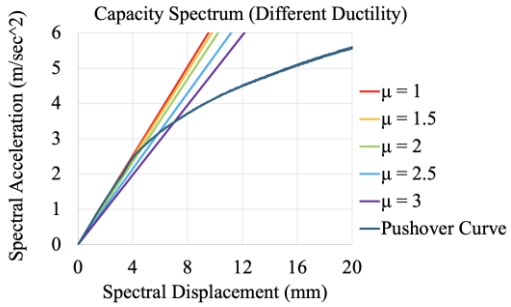

Figure 7: Capacity spectrum with different equivalent stiffness lines of URM-X.

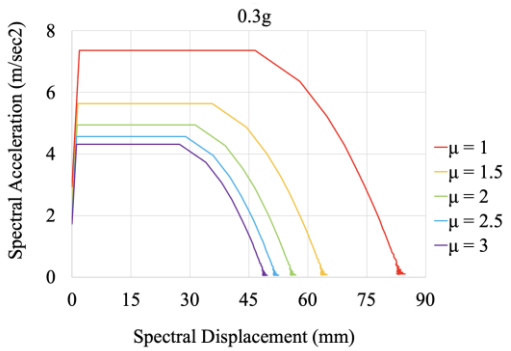

Figure 8: Demand Spectrum at 0.3g and different reduction factors.

$$PF_1 = \frac{\sum_{n=1}^{N}(w_i \phi_{i1}/g)}{\sum_{n=1}^{N}(w_i \phi_{i1}^2/g)} \quad (1)$$

$$\alpha_1 = \frac{\left[\sum_{n=1}^{N}(w_i \phi_{i1}/g)\right]^2}{\left[\sum_{n=1}^{N}(w_i/g)\right]\left[\sum_{n=1}^{N}(w_i \phi_{i1}^2/g)\right]} \quad (2)$$

$$S_a = \frac{V}{\alpha_1 \times W} \quad (3a)$$

$$S_d = \frac{\Delta_{roof}}{PF_1 \phi_{roof,1}} \quad (3b)$$

$$S_d = \frac{S_a T^2}{4\pi^2} \quad (3c)$$

where:

- PF_1 = modal participation factor for the first natural mode.
- α_1 = modal mass coefficient for the first natural mode.
- W_i/g = mass assigned to level i.
- ϕ_{i1} = amplitude of mode 1 at level i.
- N = level N, the level which is the uppermost in the main portion of the structure.
- V = base shear.
- W = building dead weight plus likely live loads,
- Δ_{roof} = roof displacement (V and the associated Δ_{roof} make up points on the capacity curve).
- S_a = spectral acceleration.
- S_d = spectral displacement (S_a and the associated S_d make up points on the capacity spectrum).

The process proposed by Otani et.al. [31] begins by identifying the first yield point of the structure, which corresponds to the spectral displacement (D_y) at a storey drift ratio of 0.07%. Initially, a ductility factor (μ) of 1 is assumed, representing a tangent to the spectral displacement axis on the capacity spectrum at the identified yield point. A line of equivalent stiffness is then drawn through the origin and the yield point, and the first performance point is identified as the intersection of this line with the demand spectrum.

Subsequently, the ductility factor is incremented to μ=1.5, and the second point on the capacity curve is determined by multiplying the yield displacement (D_y) by the corresponding ductility factor. A second line of equivalent stiffness is drawn through the origin and this new point. The equivalent damping ratio (h_e) is calculated from Equation 4 [31].

$$h_e = 0.25\left(1 - \frac{1}{\sqrt{\mu}}\right) + 0.05 \quad (4)$$

For the first mode, h_e is assumed to be 0.05 at the damage-initiation limit state, where the structure behaves elastically. The demand spectra for this limit state are prepared using a 5% damping ratio. At the life safety limit state, the demand spectra are similarly prepared with an identical damping ratio. To account for the reduction in response, the response reduction factor (F_h) is calculated from Equation 5 [31].To account for the reduction in response, the response reduction factor (F_h) is calculated from Equation 5 [31].

$$F_h = \frac{1}{1 + 10h_e} \quad (5)$$

The reduced demand spectrum is obtained by scaling both spectral acceleration (S_a) and spectral displacement (S_d) by F_h. The second performance point is identified as the intersection of this reduced demand spectrum and the equivalent stiffness line for μ=1.5. This process is repeated for increasing ductility factors and lines are obtained, iteratively generating a series of performance points that define the demand curve.

Finally, the interaction of the demand curve with the capacity curve provides the ultimate performance points. A single performance point is determined for each Peak Ground Acceleration (PGA) level of a specific earthquake spectrum. The procedure is repeated for different PGA levels to obtain performance points for varying earthquake response spectra, which are used to generate fragility curves. In addition to this, different threshold values corresponding to various structural damage states were defined based on structural capacity considerations, as outlined in Table 4.

Table 4: Threshold drift values for damage states [33].

Damage State	Unreinforced Masonry	Reinforced Masonry
Slight Damage	0.1%	0.2%
Moderate Damage	0.13%	0.28%
Extensive Damage	0.2%	0.67%
Collapse	0.33%	1.33%

The methodology proposed by Wen et. al. [34] was employed to develop these fragility curves. The performance points were correlated with predefined damage states using a fragility function, which expresses the probability of exceeding a limit-state damage threshold for a given ground motion intensity (GMI).

The fragility function is defined in Equation 6 [34].

$$P(LS_I/GMI) = 1 - \phi\left(\frac{\lambda_{CL}^{i} - \lambda_{D/GMI}}{\beta_{D/GMI}}\right) \quad (6)$$

where:

- $P(LS_I/GMI)$ = the probability of exceeding a specific limit state at a given ground motion intensity (GMI).
- $\phi(\,)$ = the standard normal cumulative distribution function.
- λ_{CL}^{i} = ln (median storey drift for a particular limit state, i).
- $\lambda_{D/GMI}$ = ln (calculated median demand storey drift given the GMI from the best-fit power-law line).
- $\beta_{D/GMI}$ = the demand uncertainty
- GMI = Ground Motion Intensity in g.
- n = Number of performance points.

Herein, the mean and standard deviation parameters are computed from Equation 7 [34].

$$\lambda_{D/GMI} = \ln(a_1) + a_2\ln(GMI) \quad (7a)$$

$$\beta_{D/GMI} = \sqrt{\frac{\sum_{k=1}^{n}[\ln(GMI_k) - \lambda_{GMI}(GMI_k)]^2}{n-2}} \quad (7b)$$

where a_1 and a_2 are constants derived from linear regression analysis of the logarithmic relationship between storey drift and GMI in terms of PGA. A series of input parameters from different ground motions were provided to create the linear plot and determine the threshold values.

The fragility curves were generated by plotting the probability of exceeding the threshold value against various GMI levels. These curves effectively depict the likelihood of the structure reaching or surpassing specific damage states under seismic loading conditions, providing valuable insights into structural vulnerability and performance.

RESULT AND DISCUSSION

Eigenvalue Analysis

A modal analysis was carried out before the pushover analysis to understand the dynamic behaviour of the structures. The time periods for all three models were calculated, providing insights into their vibration characteristics. The modal analysis results presented in Table 5 show that the time periods for the URM and JM models are quite similar within a reasonable margin of error. This indicates that the overall stiffness and dynamic characteristics of the URM and retrofitted JM structures remain comparable. However, the RM model shows noticeably shorter time periods across all three modes, reflecting a significant increase in stiffness due to the addition of reinforced concrete bands and vertical reinforcements. Furthermore, all the models showed the direction of 1st mode in the transverse direction.

Table 5: Time period of the three models in the first three modes of vibration.

Mode	Time Period (s)		
	URM	JM	RM
1st	0.35	0.32	0.21
2nd	0.29	0.26	0.18
3rd	0.23	0.21	0.16

Pushover Analysis

Pushover Curve

The peak base shear values in the X-direction for the URM-X, JM-X, and RM-X building models are obtained as 725 KN, 955 KN, and 1165 KN, respectively, at a drift level of 2.27% as shown in Figure 9 (a). Similarly, in the Y-direction, the peak base shear values for the URM-Y, JM-Y, and RM-Y models are obtained to be 495 KN, 662 KN, and 836 KN, respectively, at the same drift level as shown in Figure 9 (b). The observed behaviour shows that the base shear of the URM and JM models is nearly identical up to a displacement of 0.02 m. However, between 0.02 m and 0.04 m displacement, the JM model surpasses the URM model, with a significant increase in base shear observed at a later displacement of 0.08 m. This indicates that while gabion wire reinforcement has minimal impact on base shear during the initial stages of displacement, it substantially enhances base shear capacity in the later stages. Further, the RM model consistently demonstrates higher base shear throughout the displacement range. The integration of vertical reinforcement and horizontal bands in the RM model contributes to a significant improvement in base shear capacity from the beginning to the peak drift level, underscoring the effectiveness of reinforcement in enhancing structural performance. A similar result regarding the impact of reinforcement in stone mud masonry structures was also achieved in studies made by Ban et. al. [29] and guidelines for masonry structures [12].

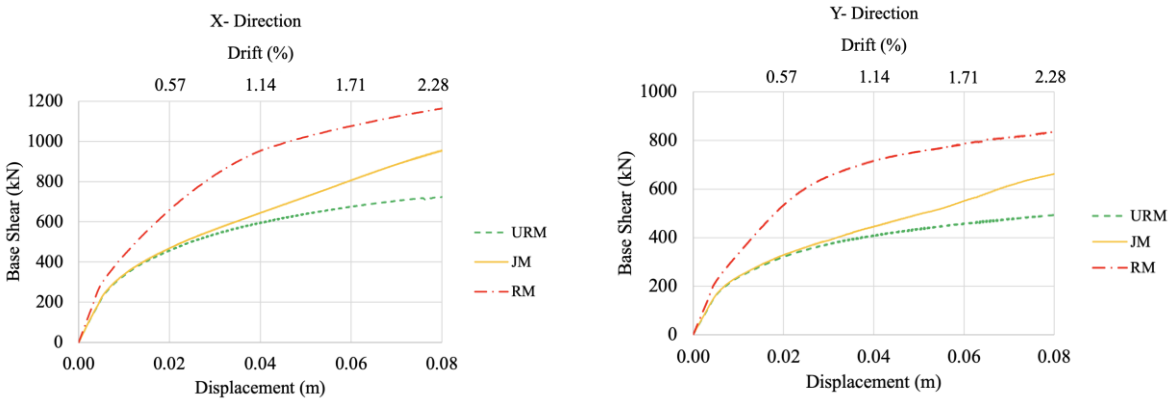

Figure 9: Pushover curve for URM, JM, and RM in a) X-direction and b) Y-direction.

Cracking Mechanism

Crack width is calculated by multiplying the crack strain (which is the total strain minus the elastic strain) by the crack bandwidth, summing the crack strains over all cracks in an element [22]. Tables 6 and 7 highlight the maximum crack widths for unreinforced masonry (URM), jacketed (JM), and reinforced (RM) models under pushover analysis at various drift levels in the X and Y directions. The X-direction, representing the longer wall length, includes multiple openings, whereas the Y-direction, the shorter wall, has only one door. At lower drift levels (e.g., 0.2%), crack widths were minimal, with URM showing the highest values (1.44 mm in X-direction and 1.1 mm in Y-direction), while JM and RM models showed progressively smaller cracks. As drift increased, the URM model exhibited the largest crack widths in both directions. In the X-direction, URM reached 10.71 mm at 1.33% drift, whereas JM and RM reduced the maximum crack widths to 7.83 mm and 9.4 mm, respectively. Similarly, in the Y-direction, URM showed a peak crack width of 16.17 mm at 1.33% drift, while JM and RM recorded lower values of 8.9 mm and 9.35 mm, respectively. These reductions in crack widths for JM and RM indicate enhanced stress distribution and damage control compared to URM under the same directional loading.

Table 6: Maximum Crack width for URM, JM, and RM at different drifts with Pushover in X-direction.

Drift	Roof Displacement (mm)	Max Crack (mm)		
		URM-X	JM-X	RM-X
0.2%	7.02	1.44	1.34	1.06
0.28%	10.03	2.35	2.17	1.61
0.66%	23.4	6.02	4.33	4.22
1.33%	46.8	10.71	7.83	9.4

The crack width for the RM model is consistently smaller than both the JM and URM models. However, at a drift of 1.33%, the crack width of the RM model exceeded that of the JM model. This could be due to the splitting of materials or the inability of the crack to propagate further due to the confinement provided by the gabion wire. This could lead to increased crack propagation at higher drift levels. This behaviour is consistent with observations in the past work of Bothara et. al [15].

Figure 10 below illustrates how the masonry units are held together by the gabion wire, which helps to restrain the cracks and prevent them from expanding beyond certain limits. However, the case may not be the same for the RM model, as, despite the band distributing stress uniformly over a large area and narrowing the crack width, at higher drift levels, the masonry units may not be held together as effectively as in the gabion wire mesh.

Table 7: Maximum Crack width for URM, JM, and RM at different drifts with Pushover in Y-direction.

Drift	Roof Displacement (mm)	Max Crack (mm)		
		URM-Y	JM-Y	RM-Y
0.2%	7.02	1.1	0.96	0.87
0.28%	10.03	2.37	2.15	1.31
0.66%	23.4	7.01	5.24	2.81
1.33%	46.8	16.17	8.9	9.35

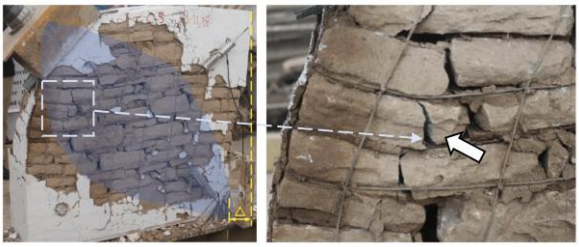

Figure 10: Splitting of masonry units at higher drift and held together by wire mesh [15].

From Figures 11-14, which display contour plots of crack width at different drift levels (with a maximum crack width of 7 mm for better visualization), Figures 11 and 12 represent the portion located at the front and right side of the structure's longer face, which includes openings, while Figures 13 and 14 depict the shorter face of the structure located at the right-hand end. In these figures, it is observed that for the URM model, cracks initiate from the corners and openings (doors and windows in the X-direction, and holes for beams in the Y-direction), gradually propagating diagonally with increasing drift. For the JM model, a similar cracking pattern is observed, but with lower crack widths and a more even distribution, indicating better stress control. In the case of the RM model, cracking did not occur in the band at these drift levels. Instead, the stress was distributed evenly across the band, preventing cracks from propagating vertically. The band acted as a confining element, preventing cracks from one level from reaching different elevations, ensuring that the cracks remained confined within the band. This behavior highlights the superior crack control and structural integrity provided by the reinforcement in the RM model.

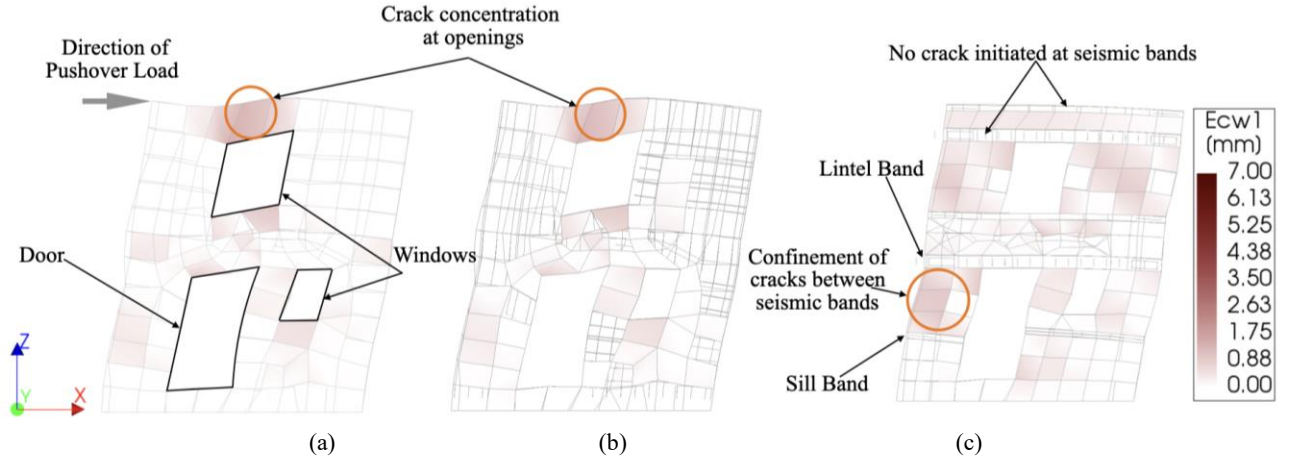

Figure 11: Crack width contour (Ecw1) at drift 0.2% in a) URM, b) JM, and c) RM in X-direction.

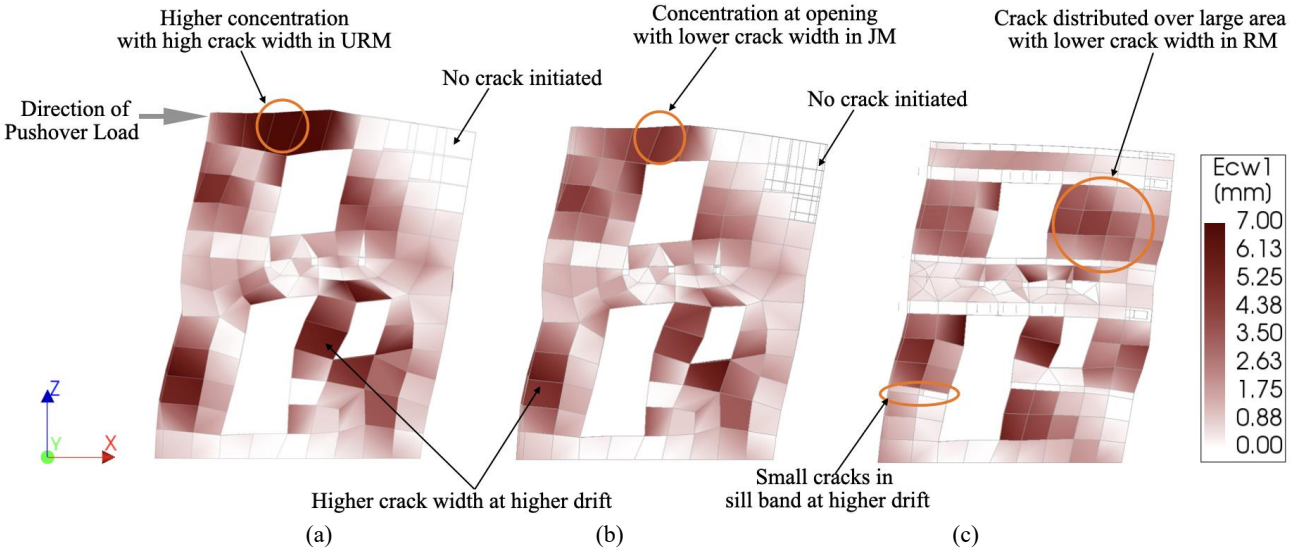

Figure 12: Crack width contour (Ecw1) at drift 1.33% in a) URM, b) JM, and c) RM in X-direction.

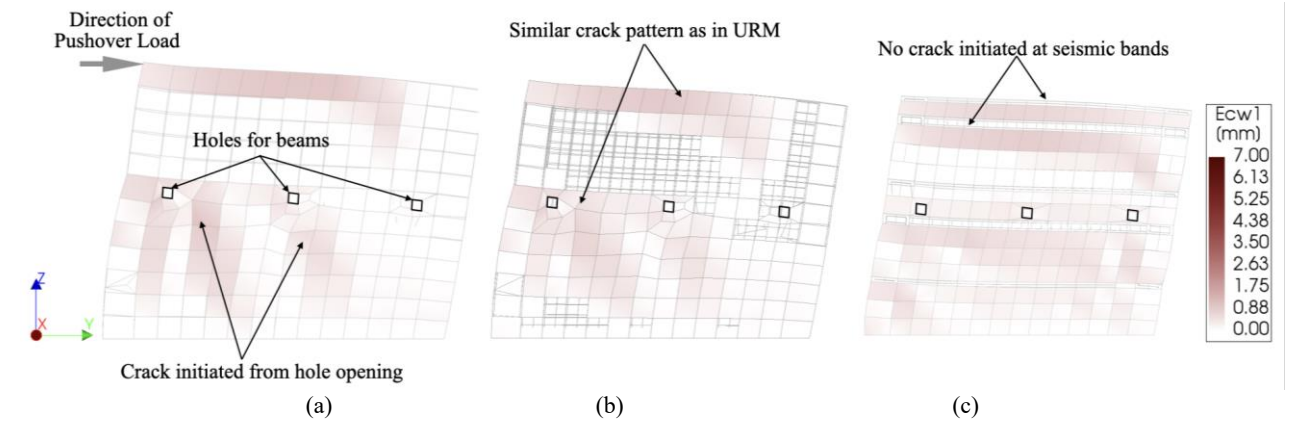

Figure 13: Crack width contour (Ecw1) at drift 0.2% in a) URM, b) JM, and c) RM in Y-direction.

Cauchy Effective Stresses

Figure 15 illustrates the distribution of SEXX for URM-Y, JM-Y, and RM-Y models at a drift of 0.2%. In the URM-Y model, stress concentrations are prominently observed at the corners and openings, indicating vulnerabilities in these regions under lateral loading. A similar pattern is observed in the JM-Y model; however, the maximum stress is notably lower, demonstrating the effectiveness of the jacketing in reducing peak stresses and distributing them more uniformly. The RM-Y model exhibits the most uniform stress distribution, with stress evenly spread due to the presence of structural elements like sill, lintel, and roof bands, which collectively enhance the rigidity and enable the structure to behave as a box-like system.

Table 8 presents the minimum and maximum Cauchy effective stresses (SEXX, SEYY, and SEZZ) for the unreinforced masonry (URM-X), jacketed (JM-X), and reinforced (RM-X) models at a drift level of 0.2% in the X-direction.

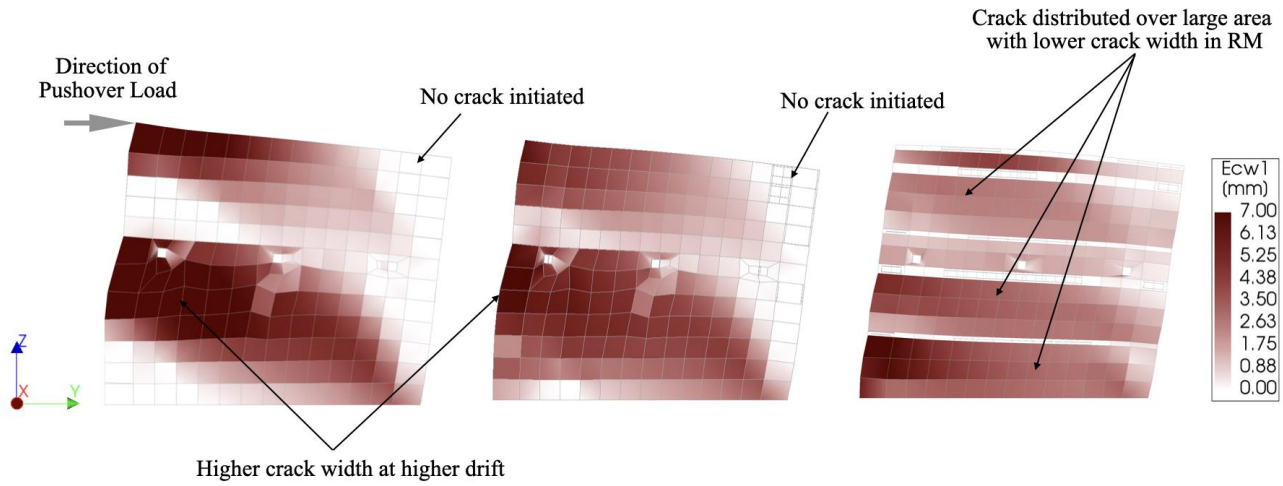

Figure 14: Crack width contour (Ecw1) at drift 1.33% in a) URM, b) JM, and c) RM in Y-direction.

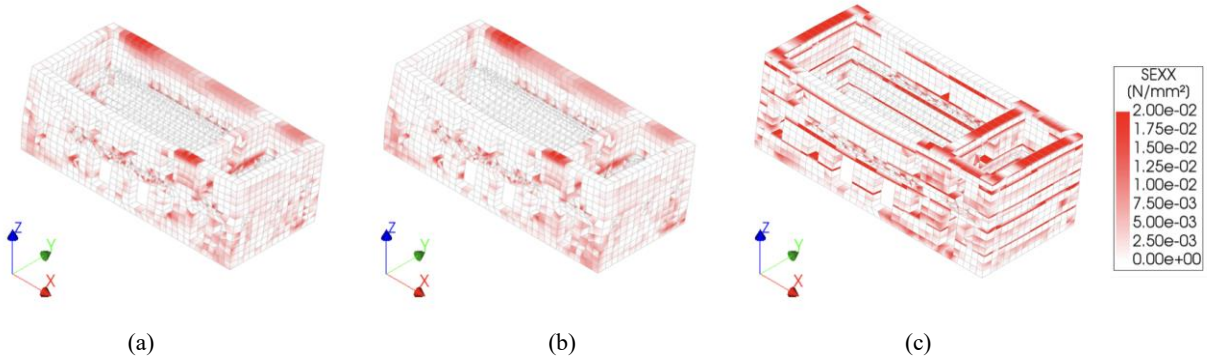

Figure 15: Cauchy Effective Stress (SEXX) for a) URM-Y, b) JM-Y, and c) RM-Y at drift 0.2%.

Table 8: Minimum and Maximum Cauchy Effective Stress at drift 0.2% (X-Direction).

Model	SEXX (MPa)		SEYY(MPa)		SEZZ(MPa)	
	Min	Max	Min	Max	Min	Max
URM-X	-0.46	0.27	-0.16	0.31	-0.28	0.52
JM-X	-3.27	2.73	-1.09	2.91	-1.32	1.42
RM-X	-4.25	3.90	-3.46	5.83	-7.40	8.11

For SEXX, the RM-X model exhibited the highest compressive and tensile stresses (-4.25 MPa to 3.90 MPa), followed by JM-X (-3.27 MPa to 2.73 MPa), while URM-X recorded the lowest stress range (-0.46 MPa to 0.27 MPa), indicating increased stiffness and load resistance in the retrofitted models. In SEYY, URM-X showed minimal stress variation (-0.16 MPa to 0.31 MPa), whereas JM-X displayed moderate values (-1.09 MPa to 2.91 MPa) and RM-X experienced a wider range (-3.46 MPa to 5.83 MPa), suggesting more active stress redistribution in reinforced and jacketed systems. For SEZZ, RM-X again recorded the highest stress range (-7.40 MPa to 8.11 MPa), followed by JM-X (-1.32 MPa to 1.42 MPa) and URM-X (-0.28 MPa to 0.52 MPa), highlighting the effectiveness of reinforcement and jacketing in enhancing load transfer and reducing stress concentrations under lateral loading.

Similarly, Table 9 presents the minimum and maximum Cauchy effective stresses (SEXX, SEYY, and SEZZ) for the URM-Y, JM-Y, and RM-Y models at a 0.2% drift in the Y-direction. The stress values for URM-Y and JM-Y are closely comparable across all components, indicating that jacketing had limited influence on stress behaviour at this drift level under Y-direction loading. In contrast, the RM-Y model showed significantly higher stress variations, reflecting increased stiffness and more active load resistance due to reinforcement. These results suggest that while jacketing offers limited benefits along directions with fewer structural discontinuities, such as the Y-direction without openings, but may be more effective where openings introduce stress concentrations, as in the X-direction. In contrast, reinforcement improves stress distribution and overall performance in both directions.

Table 9: Minimum and Maximum Cauchy Effective Stress at drift 0.2% (Y-direction).

Model	SEXX (MPa)		SEYY(MPa)		SEZZ(MPa)	
	Min	Max	Min	Max	Min	Max
URM-Y	-0.24	0.21	-0.21	0.17	-0.26	0.26
JM-Y	-0.23	0.20	-0.19	0.17	-0.24	0.27
RM-Y	-1.82	2.03	-2.05	2.78	-0.88	0.70

Capacity Spectrum Method

The response spectrum, spectral shape factor (Ch (T)) versus time period (T) for soil Type A, specified in NBC 105: 2020 [32] as shown in Figure 16 (a), is utilised in the analysis. Using the Capacity Spectrum Method, both the pushover curve and the response spectrum are converted into ADRS format Sa vs Sd, and the performance points are determined using the procedure outlined in Otani et. al. [31]. For a PGA of 0.3g in the URM-X model, the performance point is (9mm, 3.95m/sec^2) at a drift level of (0.25%), as shown in Figure 16 (b). Similarly, for the JM-X model under the same PGA, the performance point is (10.4mm, 3.77m/sec^2) at a drift level of (0.29%), as shown in Figure 16 (c). For the RM-X model, the performance point is (6.8mm, 4.35m/sec^2) at a drift level of (0.19%), as shown in Figure 16 (d). Additional performance points at various PGA levels for all models are provided in Tables 10 and 11.

Table 10: Co-ordinates of performance point of models at different ground motion intensities (X-direction).

PGA (g)	URM-X			JM-X			RM-X		
	Sa (m/s^2)	Sd (mm)	Drift %	Sa (m/s^2)	Sd (mm)	Drift %	Sa (m/s^2)	Sd (mm)	Drift %
0.10	1.93	3.13	0.09	1.99	3.59	0.10	2.12	2.52	0.07
0.20	3.08	5.65	0.16	2.96	6.41	0.18	3.39	4.43	0.13
0.30	**3.95**	**9.00**	**0.26**	**3.77**	**10.40**	**0.29**	**4.35**	**6.80**	**0.19**
0.40	4.64	12.82	0.37	4.40	14.50	0.41	5.25	9.40	0.27
0.50	5.15	16.57	0.47	4.96	18.69	0.53	6.07	11.92	0.34
0.60	5.61	20.53	0.59	5.43	23.04	0.66	6.84	14.52	0.41
0.70	6.06	24.58	0.70	5.88	27.39	0.78	7.53	17.04	0.49
0.80	6.28	28.05	0.80	6.33	31.82	0.91	8.22	19.79	0.56
0.90	6.61	32.75	0.93	6.78	36.24	1.03	8.81	22.47	0.64
1.00	6.88	36.18	1.03	7.20	40.36	1.15	9.33	25.06	0.71

**Figure 16 (b, c, d) shows the plot of parameters highlighted in bold.*

Table 11: Co-ordinates of performance point of models at different ground motion intensities (Y-direction).

PGA (g)	URM-Y			JM-Y			RM-Y		
	Sa (m/s^2)	Sd (mm)	Drift %	Sa (m/s^2)	Sd (mm)	Drift %	Sa (m/s^2)	Sd (mm)	Drift %
0.10	1.82	3.97	0.11	1.72	4.35	0.12	2.28	3.67	0.10
0.20	2.69	8.32	0.24	2.57	9.69	0.28	3.04	6.93	0.20
0.30	3.34	13.59	0.39	3.22	15.95	0.45	4.01	9.09	0.26
0.40	3.81	19.81	0.56	3.71	22.20	0.63	4.94	12.30	0.35
0.50	4.17	24.81	0.71	4.16	28.46	0.81	5.80	15.67	0.45
0.60	4.48	30.38	0.87	4.60	35.33	1.01	6.46	19.10	0.54
0.70	4.74	36.79	1.05	4.98	41.58	1.18	6.94	22.54	0.64
0.80	4.92	42.75	1.22	5.42	48.22	1.37	7.31	26.13	0.74
0.90	5.03	48.09	1.37	5.95	53.71	1.53	7.59	29.65	0.84
1.00	5.21	54.35	1.55	6.36	60.73	1.73	7.84	33.32	0.95

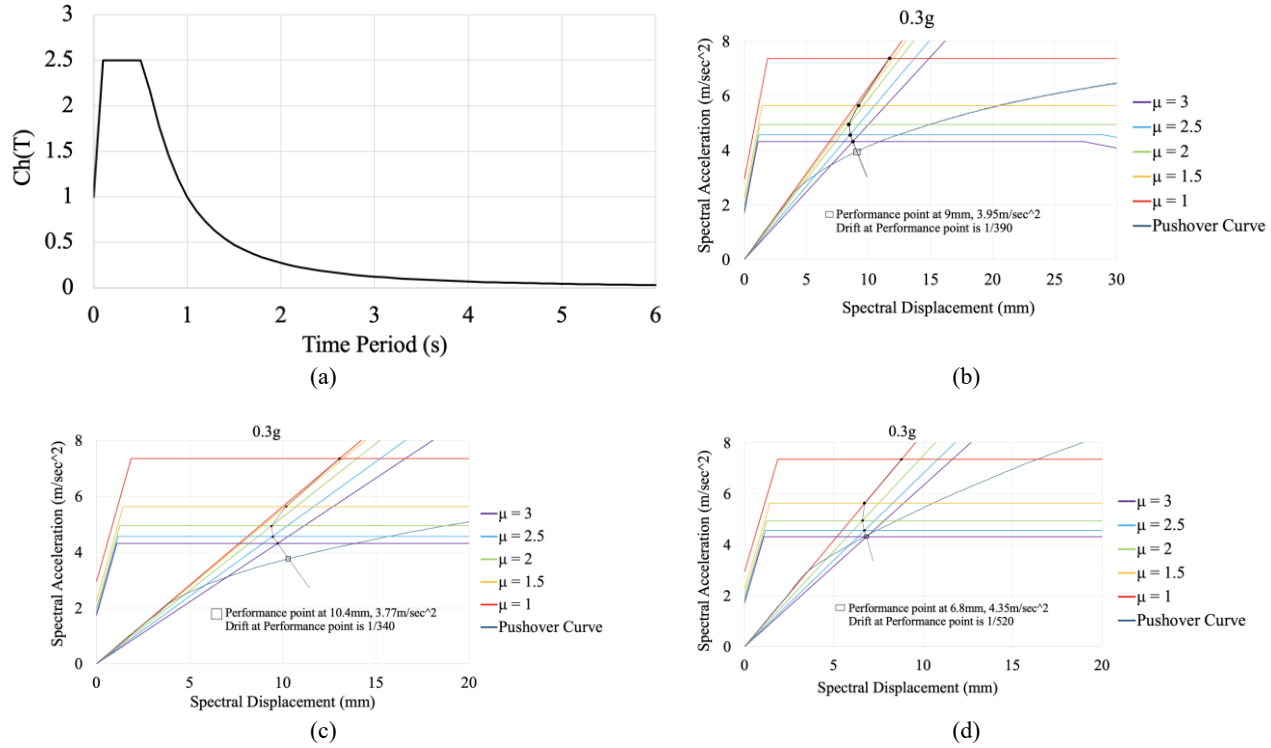

Figure 16: (a) NBC-105:2020 spectral shape factor for soil type A [32], Performance point for b) URM-X, c) JM-X, and d) RM-X for PGA of 0.3g of NBC-105:2020 spectrum soil type A.

Fragility Analysis

The performance points of all models at different PGA levels were used to plot a regression line with ln(drift) and ln(PGA), allowing the determination of $\ln(a_1)$ and a_2, which are essential for developing the fragility curve. For the URM-X model, the values of $\ln(a_1)$, a_2, and R^2 are 0.0161, 1.0955, and 0.9966, respectively, as shown in Figure 17. Similarly, the corresponding values for all other models were calculated and presented in Table 12. The fragility curves are displayed below in Figure 18 (X-direction) and Figure 19 (Y-direction) to illustrate the response of the models under varying seismic loads. Fragility curves are based on the mean and standard deviation parameters outlined above, and using damage states defined by Pema et. al. [33].

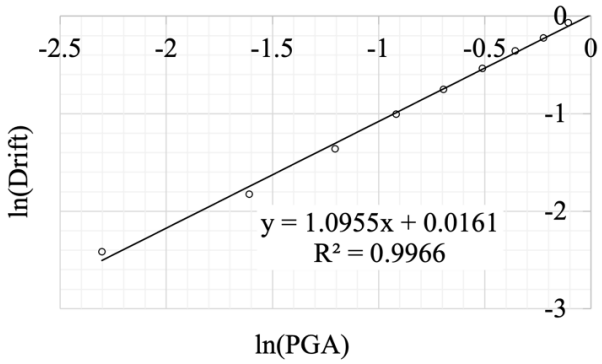

Figure 17: Regression plot for URM-X.

Between URM and JM, fragility curves reveal that JM exhibits a significant improvement in performance at the slight, moderate, and extensive damage states, demonstrating lower probabilities of exceeding these states than URM, highlighting its superior resistance to damage. JM shows exceptional performance at the collapse state due to its ductility, with a sharp reduction in the probability of collapse compared to URM. This ductility allows JM to absorb more energy and deform significantly without catastrophic failure, providing valuable time for evacuation before collapse occurs. Further, the RM model outperforms both URM and JM across all damage states, though its performance remains more uniform, with a gradual reduction in the probability of exceeding each damage state. This suggests that while RM offers consistent protection, JM's superior collapse resistance due to its ductility makes it the best option for preventing total failure in seismic events.

Table 12: Mean, standard deviation, and goodness of fit parameters for URM, JM, and RM.

Model	$ln(a_1)$	a_2	β	R^2
URM-X	**0.016**	**1.095**	0.927	**0.996**
URM-Y	0.446	1.148	1.031	0.999
JM-X	0.126	1.082	0.953	0.996
JM-Y	0.573	1.148	1.078	0.999
RM-X	-0.361	1.021	0.909	0.997
RM-X	-0.103	0.962	0.936	0.995

**Figure 17 shows the plot of parameters highlighted in bold.*

The probability of exceedance of drift states at different PGA levels for URM, JM, and RM models is presented in Tables 13 and 14. At a 0.18g PGA (reflecting the Gorkha Earthquake in 2015 at DMG station [35]), URM models exhibit a higher probability of exceeding slight and moderate damage states, particularly in the Y-direction, where the slight damage probability reaches 77.53%, and the moderate damage probability is 68.35%. As for collapse, the URM model shows a probability of 20.50% in the X-direction and 34.05% in the Y-direction, indicating a significant vulnerability to collapse, especially along the Y-direction. In comparison, the jacketed (JM) and reinforced (RM) models show a noticeable reduction

in the probability of exceeding these damage states. The JM model, for example, shows a drastic reduction from slight damage (44.97% in the X-direction) to collapse (1.70% in the X-direction), demonstrating the effective role of jacketing in reducing structural damage. Similarly, the RM model displays a more uniform reduction in damage probabilities, with lower values across all damage states, indicating the effectiveness of reinforcement in minimising damage.

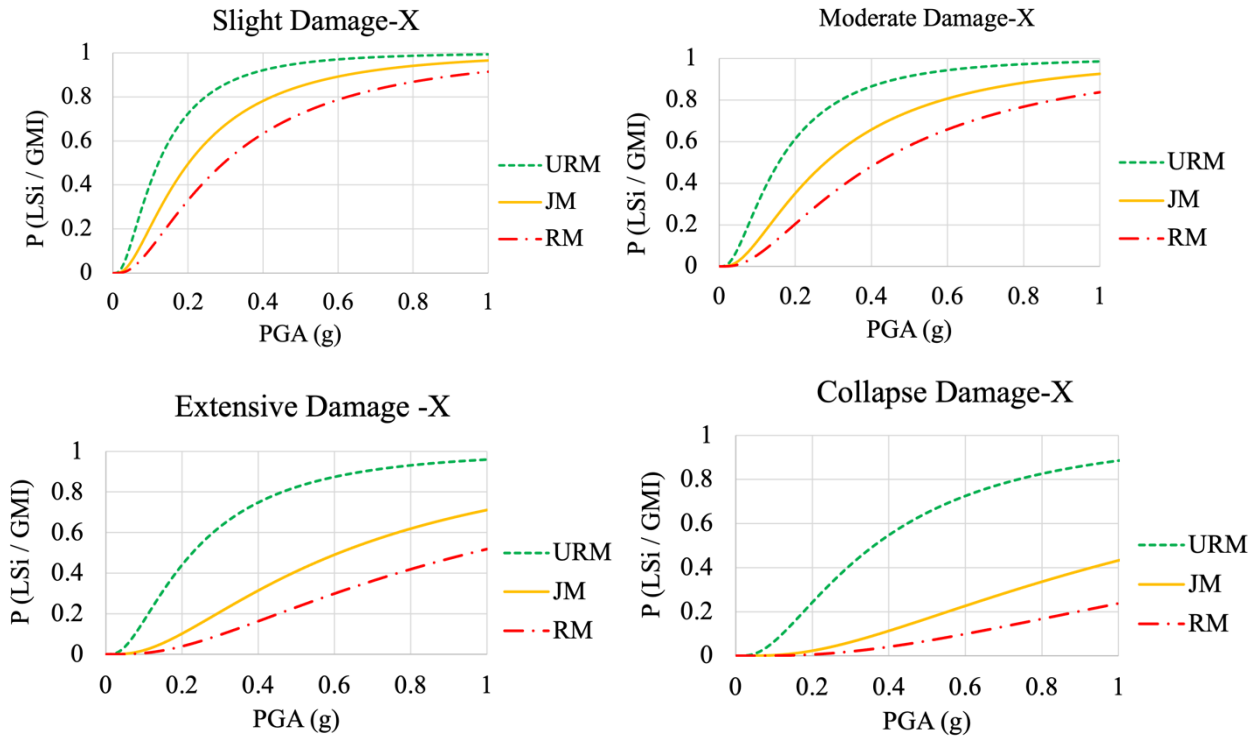

Figure 18: Fragility Curves for URM, JM, and RM at different damage states (X-Direction).

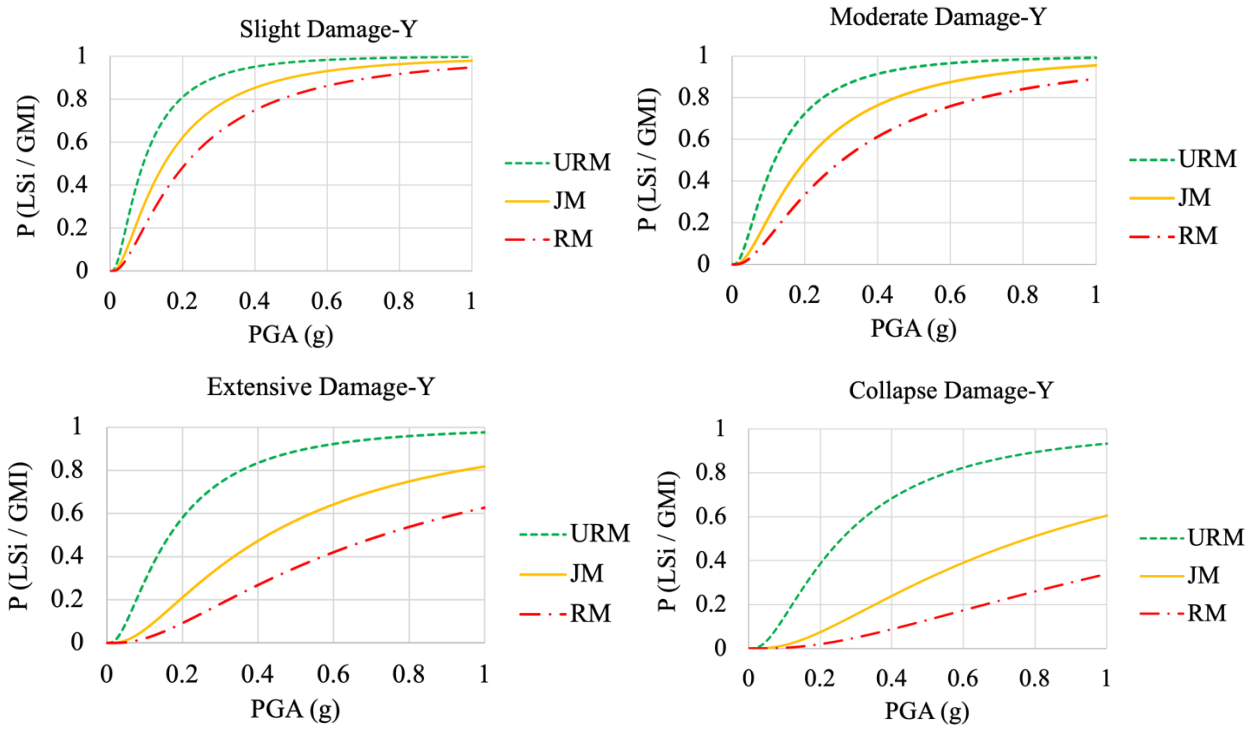

Figure 19: Fragility Curves for URM, JM, and RM at different damage states (Y-Direction).

Table 13: Probability of exceedance of drift state at 0.18g PGA (Gorkha Earthquake - 2015).

Damage state	Probability of exceedance					
	URM-X	JM-X	RM-X	URM-Y	JM-Y	RM-Y
Slight Damage	68.24%	44.97%	29.00%	77.53%	57.86%	43.89%
Moderate Damage	56.53%	30.82%	17.21%	68.35%	44.74%	29.65%
Extensive Damage	39.25%	8.20%	3.02%	53.36%	17.93%	7.50%
Collapse	20.50%	1.70%	0.41%	34.05%	5.90%	1.46%

Table 14: Probability of exceedance of drift state at 0.3g PGA (seismic zoning factor for Kaski as defined by NBC 105 2020).

Damage state	Probability of exceedance					
	URM-X	JM-X	RM-X	URM-Y	JM-Y	RM-Y
Slight Damage	85.95%	67.51%	50.82%	90.74%	77.09%	64.48%
Moderate Damage	77.87%	53.17%	35.50%	85.22%	65.95%	49.62%
Extensive Damage	62.95%	20.90%	9.61%	74.31%	35.40%	18.03%
Collapse	41.28%	6.21%	1.94%	56.26%	15.45%	4.90%

At a higher seismic loading of 0.3g PGA, as defined by the seismic zoning factor for Kaski, the damage probabilities increase across all models, but the trends remain consistent. The URM model exhibits the highest likelihood of slight and moderate damage, particularly in the Y-direction, where the probability of slight damage reaches 90.74%, and moderate damage is 85.22%. The collapse probability also increases to 41.28% in the X-direction and 56.26% in the Y-direction. In contrast, the JM and RM models show more favourable outcomes, with the JM model again showing a sharp reduction in the likelihood of collapse (6.21% in the X-direction and 15.45% in the Y-direction), while the RM model maintains lower and more uniformly decreasing probabilities across all states.

These findings suggest that gabion wire jacketing (JM) significantly reduces the probability of structural failure, especially in the more fragile URM model, with a sharp reduction from slight damage to collapse. The RM model also offers a substantial reduction in damage states, with a more gradual decrease across all damage levels. Fragility analysis shows that the Y-direction is more vulnerable to damage than the X-direction. This is mainly because the pushover capacity is higher in the X-direction, and since fragility curves are based on pushover results, this difference is reflected in the analysis. Despite its higher capacity, the X-direction faces challenges because of numerous openings and wall spans longer than the 4.5 meters permitted by NBC 202: 2015 [20], which is a potential issue.

Cost Effectiveness

The cost comparison between URM, JM, and RM models, with URM as the base model, is calculated using the material costs in the Kaski district (2081/082). For JM, two options for jacketing are considered: the first option, which includes Gabion wire jacketing only, costs NPR 100,000 (≈US$730), and the second option, which includes both jacketing and plaster, costs NPR 120,000 (≈US$880) (taking a 1:4 plaster mix). For RM, an additional band element consisting of M20 concrete and Fe415 steel adds NPR 160,000 (≈US$1170), which corresponds to its consistent protection across damage states, as indicated by its uniform performance in the fragility curves. It is important to note that these costs are in addition to the URM building's cost and do not include labour or transportation expenses, which can vary significantly depending on the location, especially in remote areas of Nepal.

Giordano et al. [18] studied the splint and bandage (S&B) retrofitting technique. Based on data from 300 buildings retrofitted by NSET and Build Change, the study highlights the incremental nature of retrofitting costs. For the S&B technique, Phase 1 costs NPR 32,000 (≈US$235, including labor cost), Phase 2 increases the cumulative cost to NPR 148,000 (≈US$1085), and Phase 3 raises it to NPR 273,000 (≈US$2000) [18]. In Phase 1, heavy-weight gable stones are replaced with lightweight roofing materials [18]. Phase 2 introduces wire mesh reinforcements at the lintel, sill level, and corners [18]. Finally, Phase 3 involves wire mesh jacketing of the remaining structural elements along with plastering in interior and exterior faces of walls [18].

The precise location of a building in relation to roads and whether these roads are paved or not has a significant impact on the overall construction cost. Transportation charges range from NPR 2,000 to NPR 4,000 (≈US$15 to $30) for short hauls, depending on the vehicle size, and can reach NPR 10,000 to NPR 18,000 (≈US$75 to $130) for long trips [18]. Labour constitutes nearly 50% of the total construction cost, making it a major expense in retrofitting projects [18]. The labour/material cost ratio is particularly high for activities such as plastering, which covers large surface areas. In stone masonry structures, additional material consumption due to uneven wall surfaces further escalates costs. The variation in labour costs across different regions of Nepal adds another layer of uncertainty to cost estimations. Further, Bothara et. al [23] highlighted that utilising local materials helps minimise costs, particularly in remote areas where isolation, especially during the monsoon, makes transportation up to three to four times costlier than the materials themselves.

Given the significant impact of transportation and labour on overall costs, a large-scale government-led retrofitting program could help reduce expenses. By implementing bulk retrofitting projects, the government can negotiate better prices for materials, reduce transportation costs, and ensure a more standardised and cost-effective retrofitting process. Such an approach would not only improve seismic resilience but also make retrofitting financially more feasible for individual homeowners.

CONCLUSION

A numerical study of the seismic assessment of stone masonry buildings, considering three models—URM, JM, and RM—was conducted using DIANA FEA to evaluate the impact of gabion wire for jacketing (JM), lintel sill roof band, and vertical reinforcement (RM). Pushover analysis was performed to generate capacity curves, which were then used to develop fragility curves through the capacity spectrum method. Based on the findings, the following conclusions can be drawn:

- Pushover analysis showed that reinforced models have significantly improved base shear capacity compared to unreinforced ones. Gabion wire jacketing shows a limited impact initially but provides substantial strength at higher displacements, while vertical reinforcement and horizontal bands consistently enhance performance throughout.
- Reinforcement bars and Gabion wire jacketing significantly reduce stress variations, as evident in the JM and RM models. While the URM model shows concentrated cracking near openings and corners, the JM model demonstrates better stress distribution and reduced crack widths. The RM model effectively confines cracks within reinforced bands, preventing vertical propagation of cracks and ensuring superior structural integrity.
- Fragility curves reveal that reinforcement significantly enhances seismic performance. The JM model exhibits improved resistance across damage states, with exceptional collapse resistance due to its ductility, allowing energy absorption and delayed failure, providing valuable time for evacuation before collapse. The RM model provides consistent protection with lower probabilities of damage across all states, underscoring its reliability in seismic events.
- At 0.18g PGA (X-direction), the URM model demonstrates significant vulnerability, with a collapse probability of 20.5%, indicating its limited capacity to withstand seismic forces. The JM model shows notable improvements, reducing the collapse probability to 1.7% and demonstrating the effectiveness of jacketing in enhancing structural resilience. The RM model performs even better, maintaining the lowest probability of collapse state i.e. 0.41%, showcasing the consistent benefits of reinforcement. At 0.3g PGA (X-direction), the URM model's collapse probability rises sharply to 41.28%, highlighting its susceptibility to higher seismic loads. In contrast, the JM model reduces collapse probability to 6.21%, reflecting its enhanced ductility and energy absorption capacity. The RM model continues to provide the best performance with consistently low damage probability of collapse state i.e. 1.94%, reinforcing its superior seismic reliability.
- When compared to the base URM model, both JM and RM models incur additional costs due to their reinforcement features. The JM model, with jacketing, is less expensive than the RM model, which includes more extensive reinforcement, such as additional bands. While the RM model offers superior performance and consistent protection across all damage states, it comes at a higher cost than JM, reflecting the more complex reinforcement structure. Both reinforced models, however, provide substantial seismic benefits over the base URM model.

In short, the reinforced models (JM and RM) show much better seismic performance than the unreinforced model (URM), with JM providing greater ductility and collapse resistance, and RM ensuring consistent protection across all damage levels. Both reinforced models provide substantial benefits over the unreinforced URM model, despite the additional costs.

It is also important to acknowledge that the current study relies on quasi-static pushover analysis, which cannot fully represent the progressive degradation and material loss typically observed in uncoursed stone masonry under severe shaking. Future work could include micro-modelling to improve the accuracy of results and analyse localised failure modes (such as delamination of walls), and non-linear dynamic analysis using real earthquake data from the region. Additionally, since fragility curves were developed based on drift and drift limit states, they may not fully capture acceleration-sensitive elements, requiring further investigation.

REFERENCES

1 Seeber L and Armbruster JG (1981). "Great detachment earthquakes along the Himalayan arc and long-term forecasting". *Earthquake Prediction: An International Review*, **4**: 259-277. https://doi.org/10.1029/me0:4p0259

2 Dhakal S, Bai L, Neupane B, Li L and Song B (2019). "Review of earthquake activity and faulting structure in Nepal Himalaya". *Bulletin of Nepal Geological Society*, **36.**

3 NPC (2015). "*Nepal Earthquake 2015 - Post Disaster Needs Assessment Vol. B: Sector Reports*". National Planning Commission, Government of Nepal.

4 Khadka B and Shakya M (2015). "Seismic characteristics of unreinforced mud masonry houses in Nepal: A miserable scenario before and after 2015 Gorkha (Nepal) earthquake". *Engineering Failure Analysis*, **124**. https://doi.org/10.1016/j.engfailanal.2021.105308

5 Ismail N, McGrannachan K and Hazelton G (2013). 'Characterisation and seismic vulnerability assessment of unreinforced masonry buildings in Dunedin CBD'. *Bulletin of The New Zealand Society for Earthquake Engineering*, **46**(3): 131-140. https://doi.org/10.5459/bnzsee.46.3.131-140

6 Bothara JK and Hiçyılmaz KMO (2008). "General observations of building behaviour during the 8th October 2005 Pakistan earthquake". *Bulletin of the New Zealand Society for Earthquake Engineering*, **41**(4): 209–233. https://doi.org/10.5459/bnzsee.41.4.209-233

7 Kafle P, Upadhyay M and Shreedhar K (2024). "Vulnerability assessment of touristic village in Nepal Himalayas: A case study of Lwang village". *Journal of Engineering Issues and Solutions*, **3**: 162-176. https://doi.org/10.3126/joeis.v3i1.67094

8 Bothara J, Ingham J and Dizhur D (2022). "Qualifying the earthquake resilience of vernacular masonry buildings along the Himalayan arc". *Journal of Building Engineering*, **52**: 104339. https://doi.org/10.1016/j.jobe.2022.104339

9 Okazaki K, Pribadi KS, Kusumastuti D and Saito T (2012). "Comparison of current construction practices of non-engineered buildings in developing countries". *15th World Conference on Earthquake Engineering*, Sep 24-28, Lisbon, Portugal.

10 Macabuag J, Guragain R and Bhattacharya S (2012). "Seismic retrofitting of non-engineered masonry in rural Nepal". *Proceedings of the Institution of Civil Engineers-Structures and Buildings*, **165**(6): 273-286. https://doi.org/10.1680/stbu.10.00015

11 NRA (2015). "*Strategic Paper on Private Housing Retrofitting after Post 2015 Gorkha Earthquake*". National Reconstruction Authority, Government of Nepal.

12 DUDBC (2016). "*Seismic Retrofitting Guidelines of Buildings in Nepal – Masonry*". Department of Urban Development and Building Construction, Government of Nepal.

13 Shrestha H, Pradhan S and Guragain R (2012). "Experiences on retrofitting of low strength masonry buildings by different retrofitting techniques in Nepal". *15th World Conference on Earthquake Engineering*, Sep 24-28, Lisbon, Portugal.

14 Wang M, Liu K, Lu H, Shrestha H, Guragain R, Pan W and Yang X (2019). "Increasing the lateral capacity of dry joint flat-stone masonry structures using inexpensive retrofitting techniques". *Bulletin of Earthquake Engineering*, **17**: 391-411. https://doi.org/10.1007/s10518-018-0454-1

15 Bothara JK, Ahmad N, Ingham JM and Dizhur D (2023). "Mechanical properties of stone masonry set in mud mortar and contained by steel wire mesh". *Construction and Building Materials*, **405**. https://doi.org/10.5459/bnzsee.41.4.209-233

16 Shrestha L, Shakya S and Norris A (2021). "Comparing seismic retrofitting approaches of traditional stone masonry in mud mortar buildings in Nepal". *VIKAS: Special Issue on Nepal's Post Earthquake Recovery & Reconstruction*, Vol. I.

17 Dhungel R, Baskota A, Gouli M, Guragain R, Tiwari A, Motra P, Pathak H, Dahal P and Shrestha P (2020). "Efforts and impacts of socio-technical assistance for retrofitting in post-earthquake reconstruction in Nepal". *17th World Conference on Earthquake Engineering*, Sendai, Japan.

18 Giordano N, Norris A, Manandhar V, Shrestha L, Paudel DR, Quinn N, Rees E, Shrestha H, Marasini, NP and Prajapati R (2021). "Financial assessment of incremental seismic retrofitting of Nepali stone-masonry buildings". *International Journal of Disaster Risk Reduction*, **60**. https://doi.org/10.1016/j.ijdrr.2021.102297

19 Dhakal R (2024). "Seismic design of buildings: Where to next?" *Bulletin of the New Zealand Society for Earthquake Engineering*, **57**(1): 1-17. https://doi.org/10.5459/bnzsee.1680

20 Nepal Building Code (2015). "*NBC 202 Guidelines on: Load Bearing Masonry*". Department of Urban Development and Building Construction, Government of Nepal.

21 Upadhyay M, Budhathoki P, Dhakal N, Tiwari L, Pun S, Barma R and Khakurel S (2024). "Seismic vulnerability assessment of historic masonry structure: A case study of Bindhyabasini temple". *15th IOE Graduate Conference*, May 17-18, Pashchimanchal Campus, Pokhara, Nepal.

22 DIANA (2025). '*DIANA FEA 10.5 User's Manual*.

23 Bothara J, Ingham J and Dizhur D (2024). "Innovative earthquake resistant school building typologies for earthquake-hit areas of Nepal". *Structures*, **70**. https://doi.org/10.1016/j.istruc.2024.107641

24 Lin YL, Fang PF, Wang X, Wu J and Yang GL (2023). "Experimental and numerical study on tensile behavior of double-twisted hexagonal gabion wire mesh". *Buildings*, **13**(7). https://doi.org/10.3390/buildings13071657

25 Adhikari RK and D'Ayala D (2020). "2015 Nepal earthquake: seismic performance and post-earthquake reconstruction of stone in mud mortar masonry buildings". *Bulletin of Earthquake Engineering*, **18**(8): 3863-3896. https://doi.org/10.1007/s10518-020-00834-y

26 Indian Standard (2000). "*IS 456 Plain and Reinforced Concrete - Code of Practice*". Bureau of Indian Standards, New Delhi, India.

27 Indian Standard (2005). "*IS 883 Design of Structural Timber in Building - Code of Practice*". Bureau of Indian Standards, New Delhi, India.

28 Endo Y and Hanazato T (2021). "Seismic assessment of two multi-tiered pagodas damaged by the 2015 Nepal earthquake". *Earthquake Engineering and Engineering Vibration*, **20**(2): 453-469. https://doi.org/10.1007/s11803-021-2031-x

29 Ban S, Shrestha KC and Bastola S (2021). "Seismic performance assessment of stone masonry buildings: Efficacy of various strengthening elements". *Journal of Building Engineering*, **96**. http://dx.doi.org/10.1016/j.jobe.2024.110380

30 Applied Technology Council (1996). "*ATC 40 Seismic Evaluation and Retrofit of Concrete Buildings*". Seismic Safety Commission, California, USA.

31 Otani S, Hiraishi H, Midorikawa M and Teshigawara M (2002). "New seismic design provisions in Japan". *Uzumeri Symposium - Behavior and Design of Concrete Structures for Seismic Performance*. https://doi.org/10.14359/11928

32 Nepal Building Code (2020). "*NBC 105 Seismic Design of Buildings in Nepal*". Department of Urban Development and Building Construction, Government of Nepal.

33 Pema, Pema and Aoki T (2020). "*Seismic evaluation and retrofitting of traditional Bhutanese stone masonry residential house*". Synopsis of IISEE-GRIPS Master Report.

34 Wen YK, Ellingwood BR and Bracci J (2004). "*Vulnerability Function Framework for Consequence-Based Engineering*". Mid-America Earthquake Centre Project, 1–101.

35 Hough SE, Martin SS, Gahalaut V, Joshi A, Landes M and Bossu R (2016). "A comparison of observed and predicted ground motions from the 2015 Mw 7.8 Gorkha, Nepal, earthquake". *Natural Hazards*, **84**: 1661-1684. https://doi.org/10.1007/s11069-016-2505-8